Characterization of vulnerable plaques by multiphoton microscopy

Magnus Borstad Lilledahl
Norwegian University of Science and Technology
Department of Electronics and Telecommunications
O.S. Bragstads Plass 2A
7491 Trondheim, Norway

Olav Anton Haugen
St. Olav's Hospital
Department of Pathology and Medical Genetics
Olav Kyrres Gate 17
7006 Trondheim, Norway
   and
Norwegian University of Science and Technology
Department of Laboratory Medicine
Children's and Women's Health
Olav Kyrres Gate 11
7491 Trondheim, Norway

Catharina de Lange Davies
Norwegian University of Science and Technology
Department of Physics
Høgskoleringen 5
7491 Trondheim, Norway

Lars Othar Svaasand
Norwegian University of Science and Technology
Department of Electronics and Telecommunications
O.S. Bragstads Plass 2A
7491 Trondheim, Norway

Abstract. Cardiovascular disease is the primary cause of death in the United States; the majority of these deaths are caused by the rupture of vulnerable plaques. An important feature of vulnerable plaques is the thickness of the fibrous cap that covers the necrotic core. A thickness of less than 65 μm has been proposed as a value that renders the plaque prone to rupture. This work shows that multiphoton microscopy (MPM) can image the plaque with μm resolution to a depth deeper than 65 μm. The fibrous cap emits primarily second harmonic generation due to collagen, in contrast to the necrotic core and healthy artery, which emits primarily two-photon excited fluorescence from elastin. This gives a good demarcation of the fibrous cap from underlying layers, facilitating the measurement of the fibrous cap thickness. Based on a measure of the collagen/elastin ratio, plaques were detected with a sensitivity of 65% and specificity of 81%. Furthermore, the technique gives detailed information on the structure of the collagen network in the fibrous cap. This network ultimately determines the mechanical strength of the plaque. A mechanical model based on this information could yield a measure of the propensity of the plaque to rupture. © *2007 Society of Photo-Optical Instrumentation Engineers.* [DOI: 10.1117/1.2772652]

1 Introduction

Coronary heart disease is the cause of the majority of deaths in the United States.[1] Most of these deaths are caused by coronary thrombosis occurring at an atherosclerotic plaque, leading to myocardial infarction.[2] Plaques prone to developing thrombosis are denoted as vulnerable plaques.[3] These plaques can lead to thrombosis either by rupture of a thin fibrous cap covering a lipid core or by erosion of the endothelium. Plaques prone to rupture are characterized by a large, lipid-rich necrotic core, covered by a thin, fibrous cap, and by infiltration of numerous macrophages.[4] The plaque cap consists mainly of collagen and a cap thickness of <65 μm has been proposed as a value that renders the plaque unstable.[5] There is currently no clinically accepted method for detecting vulnerable plaque, but numerous detection modalities are being investigated, e.g., optical coherence tomography (OCT), magnetic resonance imaging, intravascular ultrasound (IVUS), near-infrared spectroscopy and computed tomography.[3]

Autopsy studies have shown that several vulnerable plaques exist in the coronary tree in addition to the culprit lesion.[5] This has led to the hypothesis that perhaps a more-detailed stratification of plaque vulnerability is necessary to determine which plaque is the most likely to rupture. For example, polarization sensitive OCT has been proposed as an improvement over conventional OCT.[6] The birefringence of collagen in the fibrous cap will affect the polarization of the light, which can be used to infer properties about the fiber structure. Another way to collect additional information is to improve the resolution of the imaging modality. In the same way that OCT improves the resolution by an order of magnitude compared to IVUS (100 μm $\rightarrow$ 10 μm),[7] multiphoton microscopy (MPM) can improve the resolution by another order of magnitude (10 μm $\rightarrow$ 1 μm). The increase in resolution with MPM compared to OCT is accompanied by a decrease in penetration depth, usually reported to be a few 100 μm in biological tissue even though one study reported a penetration depth of 1 mm.[8]

MPM uses the nonlinear optical properties of tissue and can achieve three-dimensional (3-D) microscopy. Second-order nonlinear optical phenomena depend quadratically on the intensity of the light so that for a focused beam, the signal is generated only in a small volume around the focus, reducing out-of-focus photobleaching. The longer wavelength of

Address all correspondence to Magnus Lilledahl, Department of Electronics and Telecommunications, NTNU, O.S. Bragstads Plass 2A-7491 Trondheim, Norway. Tel: +4773591471; Fax: +4773591441; E-mail: magnus.b.lilledahl@iet.ntnu.no

the light used in MPM also increases the penetration depth compared to conventional laser scanning microscopy.

In biomedical application, the most common nonlinear effects used for microscopy are second harmonic generation (SHG) and two-photon excited fluorescence (TPEF). SHG is generated by noncentrosymmetric molecules such as collagen, and autofluorescence generated by two-photon excitation is seen from collagen, elastin, and cellular components.[9] Elastin is abundant in the media of the aorta, and collagen is the primary component in the cap of atherosclerotic plaques. MPM may thus be used to study the formation and progression of atherosclerotic plaques. In addition, it could have other applications in the management of cardiovascular disease, e.g., to monitor restenosis after stenting, and assess the effect of medication.

An advantage of MPM over regular histology is that it can be performed on intact tissue and carries the promise of *in vivo* monitoring of atherosclerotic plaques, which is of great clinical value. A catheter-based intravascular microscopy probe could be developed along the lines of existing intravascular OCT probes, but with additional scanning optics.[10] Several miniaturized, intravital microscopes for MPM have been tested.[11–15] However, for intravascular applications, further miniaturization is necessary, which could be realized by microoptical devices.

The goal of this study is thus to investigate the physiological information of the vascular structure that can be detected by MPM and to determine to what degree healthy vessels and atherosclerotic lesions can be classified compared to histological classification.[16–18] The spectral response of various tissue structures is reported, and penetration depths in tissue in various pathological states are found. Photobleaching and photodamage can be incurred in tissue during laser irradiation, and these processes are investigated as their understanding is necessary to develop a safe *in vivo* imaging modality.

2 Materials and Methods

2.1 *Materials*

Eight specimens of human aortas were excised during autopsy from eight patients (54.5 ± 10.9 years; 5 male, 3 female). The samples were put in closed containers, with some tissue paper soaked in phosphate-buffered saline (the tissue samples were not in contact with the paper tissue) and stored at $4\,°C$. Measurements were performed 1.45 ± 1.75 days after autopsy.

After microscopy, the samples were fixed in formalin and embedded in paraffin. Thin sections were cut and stained with hematoxylin-eosin-saffron (HES), elastica, and Van Gieson. HES stains cell nuclei black, cytoplasm pink, and connective fibers yellow. Elastica stains elastic fibers dark purple. Van Gieson stains muscle cells yellow and connective fibers red.

2.2 *Instrumentation*

The samples were investigated using a laser scanning inverted microscope (Zeiss LSM 510 Meta). Excitation was provided by a Ti:Sapphire laser (Coherent Mira, Model 900 F), pumped by a 5-W solid state laser (Coherent Verdi). The output of the Ti:Sapphire laser was about 750 mW, mode-locked at 800 nm. All the measurements were performed at 800 nm except the measurements described in Sec. 2.3.3, where the wavelength was tuned from 800 nm to 840 nm in 10-nm in-

crements. A plan-apochromat 40×1.2 NA water immersion objective was used in all the measurements. An acousto-optic modulator (AOM) was used to regulate the power output. A setting of the AOM at 80%, which was used in all the measurements unless otherwise noted, gave about 20 mW at the output of the objective. Laser power was measured by a Coherent LM-10 laser meter. The microscope was equiped with a Zeiss metadector, which uses a grating to disperse the generated light to 32 different channels in the spectral range from 377 nm to 710 nm at about 10-nm intervals. For all the measurements, SHG was collected at 387 to 409 nm and TPEF at 473 to 505 nm, except for the measurements in Sec. 2.3.3, where the signals were collected separately in each of the 32 channels. All measurements were performed in the reflection mode (epi-collection).

The emitted fluorescence of a solution of fluorescein ($280\ \mu M$) was measured in the microscope and compared with the one-photon fluorescence of the same solution, measured in a spectrofluorometer (Fluorolog 3 Jobin Yvon, The Horiba Group). Since the normalized spectra overlapped well with mean deviation of 5%, no further spectral calibration of the emission signals was performed.

The transmission in the system was measured by comparing the power at the laser output and at the objective for wavelengths from 800 to 840 nm to give the relative transmission,

$$T_r(\lambda) = \frac{P_{obj}(\lambda)}{P_{las}(\lambda)}. \tag{1}$$

This was used to calibrate the spectral measurements. (See Sec. 2.3.3 for details.)

2.3 *Study Protocol*

2.3.1 *Sample preparation*

The aorta samples were cut into pieces of about 5×5 mm for microscopic investigation. Out of the 8 aorta specimens, a total of 24 smaller samples were obtained. The samples were placed in a glass well with the lumen side of the vessel facing the coverslip. In the following, x and y will refer to the axes parallel to the lumen and z to the axis perpendicular to the lumen.

2.3.2 *Image collection*

Selection of measurement sites. The sample holder was placed in the microscope and a scan over an area covering $2.3\ \text{mm} \times 2.3\ \text{mm}$ was carried out. Based on these images, three primary measurement sites were defined as well as three reference sites. The measurements in the remainder of this section and Sec. 2.3.3 were then performed on each of the primary measurement sites. The images collected at each site covered an area of $230 \times 230\ \mu m$. The reference sites were shifted $115\ \mu m$ from the primary sites, thereby covering half of the primary measurement sites, and thus served as an indication of whether any changes had occurred in the tissue during the study protocol. Images of the reference sites were collected at the beginning and end of the protocol.

Z-stack of images. At each of the primary measurement sites, a z stack of images was collected. Each image covered

230×230 μm, and frames were collected at 4-μm intervals in the z direction. The average SHG and TPEF intensities, $I_s(z)$ and $I_t(z)$, were calculated for each frame to determine how the generated signals varied as a function of z. $I_s(z)$ and $I_t(z)$ were normalized by dividing by their maximum value, $I_{s,max}$ and $I_{t,max}(z)$, respectively,

$$I_{s,norm}(z) = \frac{I_s(z)}{I_{s,max}}, \quad I_{t,norm}(z) = \frac{I_t(z)}{I_{t,max}}. \quad (2)$$

The depth z where $I_{s,norm}(z)$ and $I_{t,norm}(z)$ had dropped to e^{-1} was determined.

At structures within the stack that were deemed interesting, single plane images were collected at higher resolution and longer acquisition times.

At a slice approximately 25 μm below the surface, the number of pixels covered by fibrous structure was counted. This depth was chosen so that no surface would be present in the images due to tilted image plane or surface irregularities and to ensure that the signal was still strong. A few images were manually investigated to determine the background signal. The background signal was defined as the signal level in regions of the images where no fibrillar structure could be perceived and determined to be 30 (out of 255) in the SHG images and 50 (out of 255) in the TPEF images. These values were then used as cutoff values for thresholding the images into regions containing fibrous structure and regions defined as background. The ratio of SHG to TPEF was used as a measure of a collagen-to-elastin ratio $R_{c/e}$, and was computed as the ratio of the number of pixels N with values above threshold:

$$R_{c/e} = \frac{N_{SHG}}{N_{TPEF}}. \quad (3)$$

Cross-sectional images. Cross sectional images in the x,z, and y,z planes were collected. Each line parallel to the surface was 230 μm, and each line was collected with a z interval of 0.46 μm. The gain of the detectors was increased through the scan to improve signals from deeper layers without saturating the signal at the surface.

2.3.3 Spectral response

At each primary site, the signal from one image frame was collected in each of the 32 channels of the spectral detector. The excitation light was tuned from 800 to 840 nm in 10-nm intervals. The excitation power, $P_l(\lambda_{ex})$, was measured at the output of the laser for each wavelength and the resulting spectra were calibrated by dividing by $[P_l(\lambda_{ex})T_r(\lambda_{ex})]^2$. The images were 230×230 μm. The adjustment of gain and offset were kept constant for all the spectral measurements of the samples.

2.3.4 Photobleaching and photodamage

To investigate the response of the tissue to long illumination times at various excitation powers, an area of 115 $\times 115$ μm was scanned 200 times, and the image was stored for each scan. Each scan took 1.97 s. The imaging plane was placed 10 to 20 μm under the surface. The laser power was varied from 50 to 100% in increments of 10%, which corre-

sponded to about 10 to 35 mW at the objective. If structural tissue changes were severe, the imaging series was halted before the 200 scans were completed. After the procedure had been completed, a z stack of images through the damage was collected. These images were collected with a frame size of 230×230 μm to assess the lateral and transversal extent of the photodamage.

Finite element analysis (FEM) of the thermal distribution in the tissue was performed to determine whether thermal changes in the tissue were incurred due to one-photon or two-photon absorption. Details of the analysis are given in the appendix.
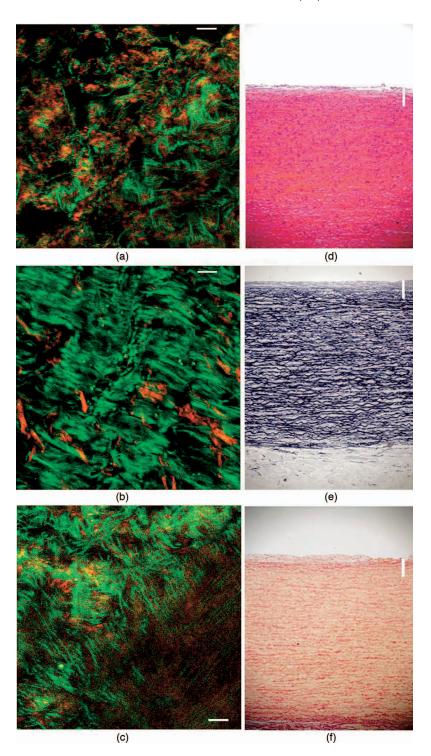
3 Results

3.1 General Features

SHG and TPEF images demonstrated different structures and distributions of connective fibers. The SHG in the images is due to collagen, and fibrous structures with TPEF, but without SHG, were interpreted as elastin. SHG is shown in red and TPEF in green in all the images. All the presented images have been processed to enhance contrast, so signal levels between SHG and TPEF can therefore not be compared directly.

Normal arteries were defined by no intimal changes observed in the histological images [see Fig. 1(d)–1(f)]. Thus, atherosclerotic lesions of type I to III according to the American Heart Association (AHA) classification are included in this group.[17] These early lesions are recognized by increased lipid content but without intimal disruptions.

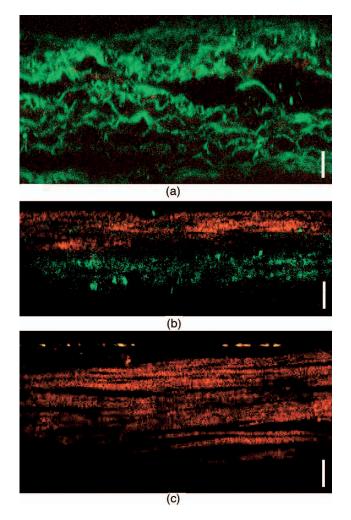In the MPM images of normal arteries, individual elastin fibers could be seen clearly down to a size of about 1 μm. The structure of the fibrous network varied, but some general features were observed. On the surface, a thin layer of elastic fibers over a layer of collagen was observed [Fig. 1(a)]. Below one or more of these layers was a layer of thicker, ordered elastic fibers with some scattered thicker collagen fibers [Fig. 1(b)]. Next, a layer of thin, ordered elastic fibers was found, where the fibers were oriented at 90 deg to the above layer [Fig. 1(c)]. In the cross-sectional images, layers of elastic lamina could clearly be distinguished [Fig. 2(a)]. The large scale images $(2.3 \times 2.3$ mm$)$ had lower resolution than the other images but yielded structure information about the connective fibers at a different size scale [Fig. 3(a)].

Atherosclerotic plaques were classified macroscopically by being clearly raised from the surrounding lumen surface and where the histological images showed the presence of a collagen cap over a lipid core [Fig. 4(d)–4(f)]. This corresponds to type V plaque in the AHA classification (fibroatheroma).

In the MPM images of the cap of an atherosclerotic plaque, the collagen appeared in thick bundles, in a nondirectional structure [Fig. 4(a)], and were different from the collagen fibers seen in the normal vessel. There was significantly more collagen in the plaque cap than in the normal aorta. Small, round, fluorescent objects of various sizes could be seen clustered in the spaces between the collagen fibers. Plaques with a macroscopically yellow color seemed to have more of these fluorescent objects, although this was not confirmed quantitatively. In one instance, the fibrous cap of a highly developed plaque was dissected, exposing the lipid core. The inside of the plaque was placed against the coverslip, and the resulting image is shown in Fig. 4(b). Many fluorescent objects with

Fig. 1 MPM images of normal vessel in the *x, y* plane (green is TPEF and red is SHG) and corresponding histological images in the *x, z* plane. (a) Normal vessel at the surface. There is a thin layer of elastic fibers over a layer of thin, wavy collagen fibers. The dark areas are regions where the wavy surface is below the image plane. (b) A dense layer of relatively thick, ordered elastic fibers was usually seen below the layers of thinner elastic fibers at the surface. Thick, randomly oriented collagen fibers can be seen between. Not the same sample as in (a) and (c). Image taken 20 μm below the surface. (c) Image taken 17 μm below the image in (a). Several layers can be seen because they are at an angle to the image plane. The deepest structure is oriented 90 deg to the layer above. Figures (d) to (f) show histological sections of normal aorta at 10×. (d) HES stain. (e) Elastica stain where the elastica laminas can be clearly seen. (f) Van Gieson stain. Connective fibers are stained red. Bars are 20 μm in the MPM images and 200 μm in the histology images.
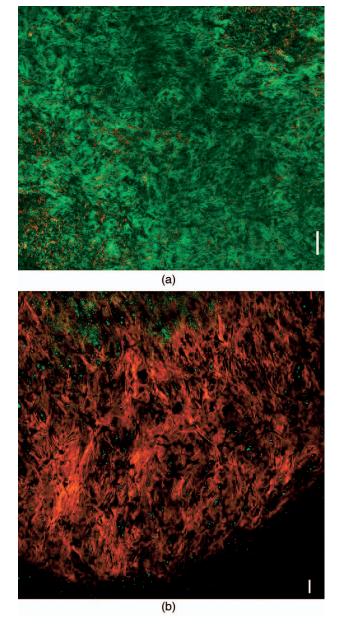
Fig. 2 Cross-sectional images (x, z plane). Green is TPEF and red is SHG. (a) The elastic laminas of a normal aorta can be clearly seen. (b) An early lesion. Layers of collagen about 20 μm thick over elastic laminas. (c) Cross section of a thick fibrous cap. The horizontal fluorescent points at the top are at the surface of the coverslip. Collagen layers can be seen down to a depth of about 60 μm. Bars are 20 μm.
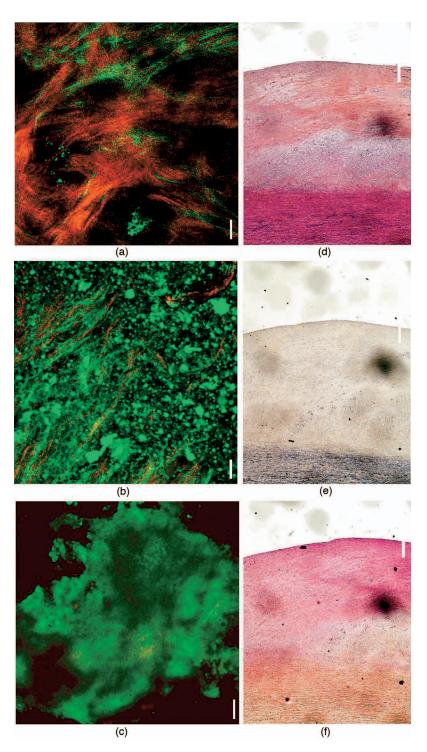

Fig. 3 These images show the structure of the fibrous networks at a larger scale than the preceding images, covering an area of 2.3 $\times$ 2.3 mm. Green is TPEF and red is SHG. (a) Normal aorta. Notice the scattered collagen fibers in the dense elastin network. (b) Atherosclerotic plaque. Notice the clusters of small fluorescent objects, clustered in the spaces between the fibers. Bars are 100 μm.

various sizes and shapes can be seen. The large-scale images also showed such fluorescent objects, and in this image, their location relative to the collagen fibers can be seen [Fig. 3(b)]. The fibers seem to have some directional orientation at this scale.

Calcified plaques (type Vb) were recognized macroscopically by very hard areas and in the histological images by an empty area surrounded by a dark purple color in the HES stained images. An MPM image of a calcification can be seen in Fig. 4(c). These areas exhibited very strong TPEF, and only a nonfibrillar structure could be seen. Some SHG could be seen within the calcification.

3.2 Spectral Response

The spectrum of collagen was obtained from an image rich in collagen, seen by strong SHG. The image obtained with 800-nm excitation was used to define regions in the image as collagen. Pixels where the SHG was greater than half of the

SHG from the pixel with the maximum value were defined as collagen. The same pixels were used to obtain the spectra at all excitation wavelengths [Fig. 5(a)].

The spectra of elastin were found by defining a region of interest (ROI) in an image where fibers exhibiting TPEF could be seen but where there was no fibrillar structure in the SHG (i.e., only background). The spectra were extracted from the pixels within this ROI [Fig. 5(b)].

A ROI that contained only the nonfibrillar structure related to calcifications was used to extract the spectra of the calcification [Fig. 5(c)]. The TPEF signal from the calcification was very strong, so excitation power was reduced by setting the

Fig. 4 (a) The cap of a thick fibroatheroma showing bundles of collagen fibers. Also notice the small fluorescent objects of unknown origin that might be autofluorescence from lipid deposits or cellular structures. (b) The inside of an atherosclerotic plaque. A large amount of fluorescent objects was seen that might be attributable to lipid droplets within the necrotic core. Also, some collagen fibers can be seen. The gain could not be adjusted separately for the SHG and TPEF signals, so to get adequate SHG signal, some of the autofluorescence saturated. (c) Calcified plaques showed strong nonfibrillar autofluorescence. Some SHG can be seen that seems to emanate from within the calcification. (d) and (e) Histology of a fibroatheroma: (d) HES stain and (e) elastica stain, showing no elastic fibers within the plaque. (f) Van Gieson stain, where the red indicates the connective tissue within the cap. Bar is 20 μm in the MPM images and 200 μm in the histology images.
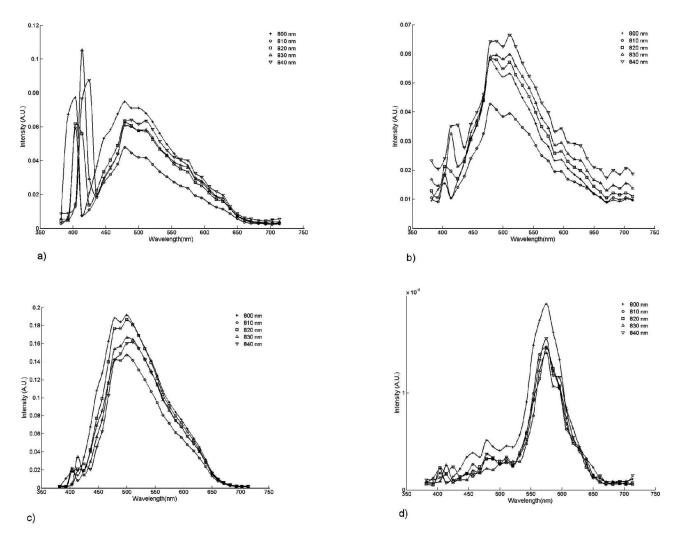
Fig. 5 Emission spectra for various tissue components, measured with different excitation wavelengths. (a) Collagen; (b) elastin; (c) calcification; and (d) fluorescent object within the fibrous cap of a plaque.

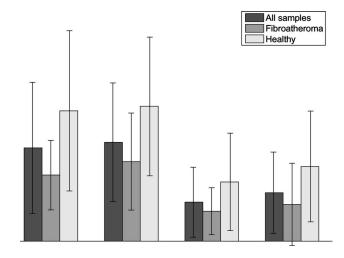AOM to 70% when measuring the spectra to avoid saturation.

The autofluorescence from the objects seen in the lipid core were strong compared to the signal from the connective tissue [Fig. 4(b)]. A spectrum of one of the fluorescent objects within the fibrous cap was extracted by defining a ROI that contained only one of these objects and is shown in Fig. 5(d). This is markedly different from the autofluorescence from the connective fibers.
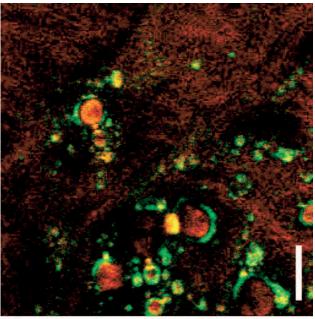
3.3 Penetration Depth

The depth where maximum signal was found and the depth where the normalized signal had fallen to e^{-1} were determined as described in Sec. 2.3.2. The samples were classified into normal vessel and fibroatheromas based on histology, according to the description in Sec. 3.1. For each of these classes, the mean values of the depth of the maximum signal and the depth where the normalized signal had fallen to e^{-1} were determined. These values are plotted in Fig. 6.

3.4 Collagen-Elastin Ratio

By defining that the presence of a fibrous cap is detected by a collagen-elastin ratio $R_{c/e}$ of greater than one, the MPM im-

Fig. 6 The mean of the penetration depth defined as the point where the signal had fallen to e^{-1} of the maximum value, and the mean of the depth where the maximum signal was found, for various vessel states. It is the difference between these two that defines the penetration depth in the sense of signal decay due to scattering and absorption. The first value indicates how deep we were able to see structures with the current experimental setup. The error bars represent the standard deviation.

Fig. 7 (a) Bubble formation in the tissue during the bleaching/heating procedure. Image is 115×115 μm. (b) Image taken 30 min after heating of the tissue, indicating that the damage incurred is irreversible and confined to the illuminated region. Image is 230×230 μm.

ages could be used to detect the presence of a plaque with a sensitivity of 65% and a specificity of 81% with histology as the reference (14 plaques and 9 normal samples; calcified plaques were excluded). Sensitivity was defined as the number of detected plaques minus the number of false negatives divided by the total number of plaques. The specificity was defined as the number of plaques detected minus the number of false positives divided by the total number of plaques. The average value of $R_{c/e}$ for samples classified as normal was 0.44, and 16.5 for plaques.

3.5   Photobleaching and Photodamage

The reference sites were displaced 115 μm from the primary measurement sites, thereby containing half of the primary measurement sites (which were 230×230 μm). No changes could be seen in these images at the end of the study protocol.

During the measurements described in Sec. 2.3.4, significant bleaching and tissue changes were incurred. After some time (up to tens of seconds, depending on the laser power), bubbles appeared in the images and increased in size with time [Fig. 7(a)]. The higher the incident powers, the earlier the bubbles appeared (within a few seconds), and the faster they grew. The z stacks of images collected about 30 min after the bleaching/heating procedure indicated that the bubbles caused irreversible damage [Fig. 7(b)]. They also showed that damage was confined closely to the illuminated area and that damage could be seen only in a layer 15 to 20 μm thick.

A finite element model of the temperature distribution in the tissue was developed (see appendix). Based on this model, it was shown that the temperature is close to the steady state temperature within one second [Fig. 8(b)]. Since the equation of heat [Eq. (4)] is linear, the shape of the time development is independent of the amount of heat generated as long as it is similarly distributed. Increasing the heat generation will raise the graph only vertically. The bubbles, however, appeared as late as after 30 to 40 s for low excitation powers. The spatial distribution of the temperature around the focus for linear absorption and second order absorption can be seen in Fig. 8(a).

Such a system, where there is a process with a given rate (defined as the inverse of the time of the appearance of bubbles) that is a function of temperature (defined to be proportional to the square of the incident power) can be described by an Arrhenius-type equation. An Arrhenius plot of the inverse of the time of bubble formation versus the inverse of the incident power squared is plotted in Fig. 8(d).
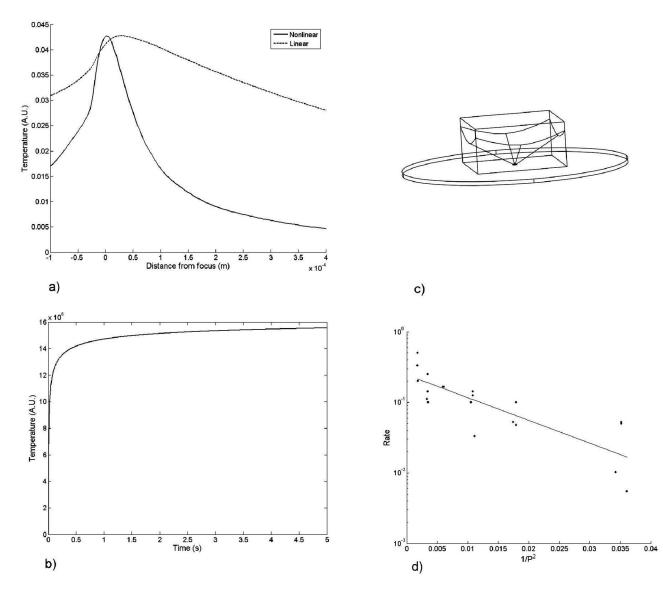
4   Discussion

4.1   Tissue Characterization

MPM can detect caps of atherosclerotic plaques without exogenous staining, and with good contrast compared to healthy vessels. Images can be collected down to a depth of >65 μm, providing a measure of one of the key features of vulnerable plaques. Three-dimensional images with μm resolution of the structural protein network can be generated without having to cut numerous histological sections, yielding important information on the mechanical strength of the cap.

SHG is, in biological tissue, generated by fibrillar collagen only in biological tissue.[19] The strong SHG from the plaque cap, known to be rich in collagen I and III, confirms this [Fig. 2(b)].[18] We have therefore assumed fibrillar structure producing SHG to be collagen. The SHG that can be seen in the spectra other than collagen could be background signal generated at various surfaces within the optical system, as SHG is known to be generated at interfaces [Fig. 5(b) and 5(c)].

TPEF, on the other hand, is seen from many biological structures. The autofluorescence spectra of elastin and collagen are very similar [Fig. 5(a) and 5(b)]. This is in agreement with another study that found significant spectral over-

Fig. 8 (a) Temperature close to focus calculated by the finite element method. Since the thermal changes in the tissue were localized to about 15 to 20 μm, the thermal shape of the nonlinear absorption better describes this observed effect. Also notice that the maximum for the linear absorption is displaced from the focus. Since the beam is scanned over an area that is much larger than the focus, the area scanned by the beam increases significantly only after the cone of the beam has become on the order of the scanned area. (b) Time dependence of the temperature at the focus, calculated with the finite element model, with nonlinear absorption causing the heating. It is clear that the temperature is very close to the steady state value after only one second. However, bubble formation was at low excitation power first observed at times of around 40 s. This indicates that there is a significant time delay between the observed phenomena (bubbles) and the onset of steady state temperature. (c) Geometry used in the FEM simulation. The disk represents the coverslip, the box is the tissue sample, and the cone inscribed in the box defines the area with heat generation. (d) An Arrhenius plot where the rate is defined as the inverse of the time of bubble formation and the temperature is assumed to be proportional to the square of the excitation power.

lap in the autofluorescence from collagen and elastin.[20] This study[20] reported that elastin had a fluorescent peak at 495 nm and cellular components at 510 nm.[20] These peaks can be seen in our spectra but are present in both collagen and elastin spectra, rather than directly related specifically to elastin or cellular components (Fig. 5). Based on the abundance of autofluorescent fibers in a healthy elastic artery (Fig. 1) and previous studies on cardiovascular structures,[20,21] fibrous structures without SHG but with TPEF were classified as elastin. Another study on atherosclerotic mice found that collagen had autofluorescence in the blue part of the spectrum, whereas elastin gave autofluorescence covering a wider spectral range,

which does not agree with our results.[21] TPEF without SHG was seen from some fibers in the plaque cap [Fig. 4(a)]. This autofluorescence seemed to come from the surface of the collagen fiber bundles. Whether this is due to elastin fibers or collagen not generating SHG has not been determined.

The thin, disorganized elastic fibers seen at the surface of the healthy vessels probably belong to the subendothelial connective tissue, while the thicker ordered layers are the elastic lamina [Fig. 1(a)–1(c)]. Scattered collagen fibers can be seen, apparent in Fig. 3(a).

The structure of the fibrous cap could be imaged at several levels of detail [compare Fig. 4(a) and Fig. 3(b)]. This fibrous

structure is directly related to the mechanical strength of the plaques and might yield some insight into why some plaques rupture and others do not. The structure of the collagen fibers can perhaps also be used to better understand the nature of the signals collected by polarization-sensitive OCT.

The origin of the fluorescent objects seen in the fibrous caps and lipid cores have not been determined but could arise from several sources. In the plaques, the objects seem to be clustered in small groups between the collagen fibers [Fig. 4(a)]. This could be foam cells (macrophages with intracellular lipid droplets). The lipid core is mainly necrotic, and the fluorescent objects seen here appear in different sizes, which could be related to extracellular lipid droplets [Fig. 4(b)]. The abundance of the fluorescent objects within the yellow plaque and within the plaque core supports the hypothesis that these objects are related to lipid-related substances. Blankenhorn reported strong, green, one-photon autofluorescence from the lipid core of atherosclerotic plaques and related this to carotenoids, which are known to be lipophilic.[22] Another study found one-photon autofluorescence from various biochemical components known to be present in atherosclerotic plaques, e.g., oxidized lipoproteins and cholesterol esters, further supporting the hypothesis that the TPEF signal is related to lipid-rich substances in the plaques.[23] The autofluorescence from some of the unidentified objects that were observed in the plaque caps had a fluorescent peak at 575 nm [Fig. 5(d)]. Since the images collected in this study, except the spectral measurements, measured the fluorescence in the interval from 473 nm to 505 nm, the objects with a fluorescent peak at 575 were probably not detected. The strong TPEF from the lipid core could further enhance the demarcation between the fibrous cap and the lipid core. However, all the plaques imaged in this study had plaques thicker than the penetration depth of the system, so this was not confirmed.

The spectral calibration of the metadetector with fluorescein was limited by weak signals below 475 nm and above 625 nm, so inaccuracies might exist in these parts of the spectra. Furthermore, since the spectra were generated at different depths and the excitation power decreases with depth, the intensity of the measured spectra cannot directly be compared.

The technique was able to differentiate normal vessels from atherosclerotic plaques based on the collagen/elastin ratio with fairly good sensitivity and specificity (65% and 81%, respectively). Since collagen also gives TPEF, one could argue that the ratio $R_{c/e}$ actually measures the ratio of pixels with collagen compared to pixels with either collagen and elastin. However, the fluorescence from collagen was generally weaker than the threshold value we used, which can be appreciated from the fact that the ratio for collagen-rich tissue had a value greater than one (average 16.5 for plaques). The erroneous classifications were due to some samples with high collagen content in the intima even though they appeared normal in the histological sections. In one instance, the fibrous cap was visible only down to a depth of 20 μm in the MPM images, even though a thick cap was seen in the histology. This also generated an erroneous classification. A limitation of these values is that the same observer performed both classifications and was blinded only to the histological results and not vice versa. Another limitation of the study is that the

position of the MPM measurements and histological sections are not necessarily colocalized in the samples.

The collagen/elastin ratio, $R_{c/e}$, could be calculated for each layer in the vessel wall yielding an image of the fibrous cap since this type of tissue has a much higher value of $R_{c/e}$ compared to the normal vessel. An important feature of $R_{c/e}$ is the large difference in its value between the vessels classified as normal and those classified as plaque, mean values of 0.44 and 16.5, respectively. This is more than an order of magnitude difference in the signal and could yield improvements over methods like OCT and ultrasound, where contrast in the signal between different tissue types is often a limiting factor.

Imaging was achieved down to a depth of about 100 μm, which represents the upper layers of the relatively thick aorta (2 to 3 mm) (Fig. 6). The coronary arteries are much thinner, so more of the vessel anatomy could be imaged. The penetration depth in tissue is determined by scattering, which reduces the power at the focus, and dispersion, which degrades the pulse shape at the focus. The effect of scattering can be reduced by using an objective with a smaller numerical aperture, albeit at a loss in resolution. However, the generated signal will be lower since a less tight focusing will reduce field intensities, resulting in weaker second-order processes. The best trade-off will thus depend on the resolution necessary for the application at hand.

Since scattered photons do not affect the collected signal (as they do in OCT), the loss due to scattering can to some degree be compensated for by increasing the excitation power. Of course, availability of laser sources and heating due to linear absorption will limit this approach. However, as was observed in this study, the heat damage seems to arise from a second order process, so the reduction in light at the focus due to scattering can be compensated for by increasing the incident power without creating tissue damage.

The penetration depths reported in this study do not necessarily compare to *in vivo* values. As described by Zoumi et al., the fiber structure changes significantly under physiological pressures and thereby also the scattering.[20] Also, the present study investigated the aorta, and values for the coronary arteries could be different. One feature of vulnerable plaques is a fibrous cap thinner than 65 μm, so this feature of vulnerable plaques can be detected with MPM.

4.2 Photobleaching and Photodamage

Significant photobleaching was observed during the procedure described in Sec. 2.3.4. Photobleaching was seen to strongly affect the TPEF signal. The SHG signal also decayed during the procedure, albeit at a slower rate. After a certain time (up to tens of seconds) dependent on the incident power, bubbles appeared in the images. The physics of bubble formation from plasma generation has been described in great detail in several papers.[24,25] Dynamics of plasma formed bubbles are on a time scale of μs. However, the bubbles we see appear up 30 s after start of the irradiation and grow at relatively slow rates, indicating that we are dealing with a different type of process. Several studies on the biological safety of pulsed laser irradiation have investigated the viability and effect on cells after irradiation.[26,27] However, the results in Fig. 7 indicate there is also the possibility of severe changes in the extracellular matrix that might have an effect on the clinical safety of the

technique. The photodamage was incurred in a very narrow region, only 15 to 20 μm deep, indicating that the damage arises from second order absorption. This can be appreciated from the spatial dependence of the temperature determined from the finite element model [Fig. 8(b)], where the assumption of second order absorption better describes the extent of the photodamage. Using reported values of linear absorption in the aorta yielded a maximum temperature increase of 2.3 K after 200 s. In this case, we assumed that convection at the upper surfaces kept the surface temperature close to the temperature of the surrounding air, so fixed temperature was used as the boundary condition. We also used thermal insulation as the boundary condition for all the surfaces, resulting in a temperature increase of 8.8 K after 200 s. These temperatures seem too small to generate the observed bubble formation, further indicating that nonlinear absorption is the primary source of the damage. This is in agreement with other studies, where they found that the damage to the tissue followed a $P^{2.5}$ relation with the incident power.[26,27]

The bubble formation could be due to gas release of absorbed gases in the tissue due to the reduction in the amount of gas that can be dissolved in the tissue with increasing temperature. This process must be well understood before a clinical tool can be developed so that excitation powers can be kept well within safe levels.

5 Conclusion

MPM can assess tissue structure at a resolution not achievable by other imaging modalities for atherosclerotic plaque. The fibrous cap can be imaged to a depth of >65 μm with good contrast compared to underlying layers, thereby measuring one of the key characteristics of vulnerable plaque. The mechanical stability of a vulnerable plaque is directly related to the likelihood of rupture. The network of collagen fibers is what determines the mechanical stability, and this can imaged by MPM.

Several characteristic physiological features of vessels can be seen with MPM, e.g., elastic lamina and collagen fibers in the plaque cap. All images in this study were collected in the reflection mode, and the technique can therefore be transferred to an *in vivo* intravascular imaging modality. The information could have important applications, both clinically, and in pathophysiological research.

Acknowledgments

Appendix: Finite Element Model

An FEM model was used to find the temperature distribution in the samples during irradiation. Commercial software (Comsol Multiphysics, Comsol AB, Sweden) was used to perform the analysis. Default settings for mesh densities and solvers were used.

The equation to be solved to find the temperature T is the heat equation,

Table 1 Thermal properties used in the FEM model.

Material	Thermal Conductivity κ (W/m·K)	Specific Heat c_p (J/kg·K)	Density ρ (kg/m^3)
Tissue	0.4	4000	1000
Glass	0.8	800	2600

$$\nabla^2 T - \frac{1}{\chi} \frac{\partial T}{\partial t} = -\frac{q}{\kappa}, \qquad (4)$$

where $\chi = \kappa/\rho c_p$ is the diffusivity, κ is the thermal conductivity, ρ is the density, and c_p is the specific heat; see Table 1 for the values used in the model. q is the heat generation per unit volume per unit time; see the following for values used.

A water immersion objective with NA$=1.2$ was used in the measurements, and this yields a cone of illumination with an angle to the illumination axis of about 60 deg. We will assume that the shape of the beam is a perfect cone so that the radius of the cone is given by $r = \sqrt{3}\Delta z$, where Δz is the distance from the focus. This geometrical optics approximation to the light distribution is not valid near the focus, but since we are scanning the beam over a large area and looking only for approximate solutions, the details of the light distribution near the focus is not important. Since the beam is scanned over an area with sides $a = 115$ μm, the total area illuminated by the beam at a distance Δz from the focus is $A_t = \pi(\sqrt{3}\Delta z)^2 + a^2 + 4\sqrt{3}\Delta za$. The area of a cross section of the cone perpendicular to the illumination axis is $A_c = \pi(\sqrt{3}\Delta z + 0.25$ μm$)^2$. The term 0.25 μm is added for the finite waist size of the beam at the focus.

The change in intensity due to absorption in a layer Δz (i.e., the heat generated per area per time) is given by $\Delta I = \mu_a^{(1)} I \Delta z$, where $\mu_a^{(1)}$ is the linear absorption coefficient. Since $I = P/A_c$, the heat generated per unit volume per unit time is then

$$q = \frac{\Delta I A_c}{A_t \Delta z} = \frac{\mu_a I \Delta z A_c}{A_t \Delta z} = \frac{\mu P(z)}{A_t}. \qquad (5)$$

For two-photon absorption, the absorption is quadratic in the intensity, so $\Delta I = \mu_a^{(2)} I^2 \Delta x$, where $\mu_a^{(2)}$ is a nonlinear absorption coefficient. The heat generated per unit volume per unit time is then

$$q = \frac{\mu^{(2)} P(z)^2}{A_c A_t}. \qquad (6)$$

Equations. (5) and (6) were used for the heat generation in the FEM models. Since the beams are focused and not collimated, the absorption coefficients should include a factor between 1 and 2 due to the increased path length, but this was not taken into account. The reported values should be interpreted with this in mind. Linear absorption and scattering coefficients of human aorta tissue are $\mu_a = 80$ m^{-1} and $\mu_s = 250$ m^{-1} (Ref. 28). Values reported in the literature vary, but we have used the highest value found. The power as a function of distance from glass/tissue interface z was thus described by $P = P \exp[-(\mu_a + \mu_s)z]$.

The geometry [see Fig. 8(c)] consisted of a disk with radius 5 mm, thickness 170 μm, made of glass, representing the coverslip. The tissue was modeled as box with sides $4 \times 4 \times 2$ mm, with the light cone inscribed. The boundary condition at the bottom of the glass was set to thermal insulation, while all other boundaries were set to constant temperature.

Using the reported value of the linear absorption coefficient yielded a maximum temperature increase of 2.3 K after 200 s. The nonlinear absorption coefficient is not known, but the normalized temperature distribution near the focus is shown in Fig. 8(a). The temperature as a function of time is shown in Fig. 8(b). The structure was also simulated with all boundaries set to thermal insulation, which resulted in a temperature increase of 8.8 K after 200 s.

References

1. T. Thom, N. Haase, W. Rosamond, V. J. Howard, J. Rumsfeld, T. Manolio, Z.-J. Zheng, K. Flegal, C. O'Donnell, S. Kittner, D. Lloyd-Jones, D. C. Goff, Jr., Y. Hong, R. Adams, G. Friday, K. Furie, P. Gorelick, B. Kissela, J. Marler, J. Meigs, V. Roger, S. Sidney, P. Sorlie, J. Steinberger, S. Wasserthiel-Smoller, M. Wilson, and P. Wolf, "Heart disease and stroke statistics–2006 update: a report from the American Heart Association statistics committee and stroke statistics subcommittee," *Circulation* **113**(6), c85–e151 (2006).
2. M. J. Davies and A. C. Thomas, "Plaque fissuring—the cause of acute myocardial infarction, sudden ischaemic death, and crescendo angina," *Br. Heart J.* **53**(4), 363–373 (1985).
3. R. Waksman and P. W. Serruys, Eds., *Handbook of the Vulnerable Plaque*, Taylor and Francis, London (2004).
4. C. V. Felton, D. Crook, M. J. Davies, and M. F. Oliver, "Relation of plaque lipid composition and morphology to the stability of human aortic plaques," *Arterioscler., Thromb., Vasc. Biol.* **17**, 1337–1345 (1997).
5. A. P. Burke, A. Farb, G. T. Malcom, Y.-H. Liang, J. Smialek, and R. Virmani, "Coronary risk factors and plaque morphology in men with coronary disease who died suddenly," *N. Engl. J. Med.* **336**(18), 1276–1282 (1997).
6. S. D. Giattina, B. K. Courtney, P. R. Herz, M. Harman, S. Shortkroff, D. L. Stamper, B. Liu, J. G. Fujimoto, and M. E. Brezinski, "Assessment of coronary plaque collagen with polarization sensitive optical coherence tomography (PS-OCT)," *Int. J. Cardiol.* **107**(3), 400–409 (2006).
7. M. E. Brezinski, G. J. Tearney, B. E. Bouma, J. A. Izatt, M. R. Hee, E. A. Swanson, J. F. Southern, and J. G. Fujimoto, "Optical coherence tomography for optical biopsy: properties and demonstration of vascular pathology," *Circulation* **93**(6), 1206–1213 (1996).
8. P. Theer, M. T. Hasan, and W. Denk, "Two-photon imaging to a depth of 1000 micrometers in living brains by use of a Ti:Al2O3 regenerative amplifier," *Opt. Lett.* **28**(12), 1022–1024 (2003).
9. E. Brown, T. McKee, E. diTomaso, A. Pluen, B. Seed, Y. Boucher, and R. K. Jain, "Dynamic imaging of collagen and its modulation in tumors *in vivo* using second-harmonic generation," *Nat. Med.* **9**(6), 796–800 (2003).
10. J. G. Fujimoto, S. A. Boppart, G. J. Tearney, B. E. Bouma, C. Pitris, and M. E. Brezinski, "High resolution *in vivo* intra-arterial imaging with optical coherence tomography," *Heart* **82**(2), 128–133 (1999).
11. F. Helmchen, M. S. Fee, D. W. Tank, and W. Denk, "A miniature head-mounted two-photon microscope: high-resolution brain imaging in freely moving animals," *Neuron* **31**(6), 903–912 (2001).
12. D. Bird and M. Gu, "Compact two-photon fluorescence microscope based on a single-mode fiber coupler," *Opt. Lett.* **27**(12), 1031–1033 (2002).
13. F. Helmchen, "Miniaturization of fluorescence microscopes using fiber optics," *Exp. Physiol.* **87**(6), 737–745 (2002).
14. J. C. Jung and M. J. Schnitzer, "Multiphoton endoscopy," *Opt. Lett.* **28**(11), 902–904 (2003).
15. W. Göbel, J. N. D. Kerr, A. Nimmerjahn, and F. Helmchen, "Miniaturized two-photon microscope based on a flexible coherent fiber bundle and a gradient-index lens objective," *Opt. Lett.* **29**(21), 2521–2553 (2004).
16. H. C. Stary, D. H. Blankenhorn, A. B. Chandler, S. Glagov, W. I. Insull, Jr., M. Richardson, M. E. Rosenfeld, S. A. Schaffer, C. J. Schwartz, W. D. Wagner, and R. W. Wissler, "A definition of the intima of human arteries and of its atherosclerosis-prone regions," *Circulation* **85**(1), 391–405 (1992).
17. H. C. Stary, A. B. Chandler, S. Glagov, J. R. Guyton, W. Insull, Jr., M. E. Rosenfeld, S. A. Schaffer, C. J. Schwartz, W. D. Wagner, and R. W. Wissler, "A definition of initial, fatty streak, and intermediate lesions of atherosclerosis," *Arterioscler. Thromb.* **14**(5), 840–856 (1994).
18. H. C. Stary, A. B. Chandler, R. E. Dinsmore, V. Fuster, S. Glagov, W. I. Insull, Jr., M. E. Rosenfeld, C. J. Schwartz, W. D. Wagner, and R. W. Wissler, "A definition of advanced types of atherosclerotic lesions and a histological classification of atherosclerosis," *Circulation* **92**, 1355–1374 (1995).
19. W. R. Zipfel, R. M. Williams, R. Christie, A. Y. Nikitin, B. T. Hyman, and W. W. Webb, "Live tissue intrinsic emission microscopy using multiphoton-excited native fluorescence and second harmonic generation," *Proc. Natl. Acad. Sci. U.S.A.* **100**(12), 7075–7080 (2003).
20. A. Zoumi, X. Lu, G. S. Kassab, and B. J. Tromberg, "Imaging coronary artery microstructure using second-harmonic and two-photon fluorescence microscopy," *Biophys. J.* **87**(4), 2778–2786 (2004).
21. M. van Zandvoort, W. Engels, K. Douma, L. Beckers, M. oude Egbrink, M. Daemen, and D. W. Slaaf, "Two-photon microscopy for imaging of the (atherosclerotic) vascular wall: a proof of concept study," *J. Vasc. Res.* **41**(1), 54–63 (2004).
22. D. H. Blankenhorn and H. Braunstein, "Carotenoids in man. iii. the microscopic pattern of fluorescence in atheromas and its relation to their growth," *J. Clin. Invest.* **37**, 160–165 (1958).
23. K. Arakawa, K. Isoda, I. Toshimitu, K. Nakajima, T. Shibuya, and F. Ohsuzu, "Fluorescence analysis of biochemical constituents identifies atherosclerotic plaque with a thin fibrous cap," *Arterioscler., Thromb., Vasc. Biol.* **1**, 1–71 (2002).
24. A. Vogel and V. Venugopalan, "Mechanisms of pulsed laser ablation of biological tissues," *Chem. Rev. (Washington, D.C.)* **103**(2), 577–644 (2003).
25. V. Venugopalan, A. Guerra, K. Nahen, and A. Vogel, "Role of laser-induced plasma formation in pulsed cellular microsurgery and micro-manipulation," *Phys. Rev. Lett.* **88**(7), 078103 (2002).
26. A. Hopt and E. Neher, "Highly nonlinear photodamage in two-photon fluorescence microscopy," *Biophys. J.* **80**(4), 2029–2036 (2001).
27. J. A. Galbraith and M. Terasaki, "Controlled damage in thick specimens by multiphoton excitation," *Mol. Biol. Cell* **14**(5), 1808–1817 (2003).
28. M. Keijzer, R. Richards-Kortum, S. L. Jacques, and M. S. Feld, "Fluorescence spectroscopy of turbid media: autofluorescence of the human aorta," *Appl. Opt.* **28**, 4286–4292 (1989).